

# Analytic tractography: A closed-form solution for estimating local white matter connectivity with diffusion MRI

Matthew Cieslak<sup>a</sup>, Tegan Brennan<sup>b</sup>, Wendy Meiring<sup>c</sup>, Lukas J. Volz<sup>a,d</sup>, Clint Greene<sup>e</sup>, Alexander Asturias<sup>a</sup>, Subhash Suri<sup>b</sup>, Scott T. Grafton<sup>a</sup>

<sup>a</sup>*Department of Psychological and Brain Sciences, University of California Santa Barbara*

<sup>b</sup>*Department of Computer Science, University of California Santa Barbara*

<sup>c</sup>*Department of Statistics and Applied Probability, University of California Santa Barbara*

<sup>d</sup>*SAGE Center for the Study of the Mind, University of California Santa Barbara*

<sup>e</sup>*Department of Electrical and Computer Engineering, University of California Santa Barbara*

---

## Abstract

White matter structures composed of myelinated axons in the living human brain are primarily studied by diffusion-weighted MRI (dMRI). These long-range projections are typically characterized in a two-step process: dMRI signal is used to estimate the orientation of axon segments within each voxel, then these local orientations are linked together to estimate the spatial extent of putative white matter bundles. Tractography, the process of tracing bundles across voxels, either requires computationally expensive (probabilistic) simulations to model uncertainty in fiber orientation or ignores it completely (deterministic). Furthermore, simulation necessarily generates a finite number of trajectories, introducing “simulation error” to trajectory estimates. Here we introduce a method to analytically (via a closed-form solution) take an orientation distribution function (ODF) from each voxel and calculate the probabilities that a trajectory projects from a voxel into each directly adjacent voxels. We validate our method by demonstrating experimentally that probabilistic simulations converge to our analytically computed transition probabilities at the voxel level as the number of simulated seeds increases. We then show that our method accurately calculates the ground-truth transition probabilities from a publicly available phantom dataset. As a demonstration, we incorporate our analytic method for voxel transition probabilities into the Voxel Graph framework, creating a quantitative framework for assessing white matter structure, which we call “analytic tractography”. The long-range connectivity problem is reduced to finding paths in a graph whose adjacency structure reflects voxel-to-voxel analytic transition probabilities. We demonstrate that this approach performs comparably to the current most widely-used probabilistic and deterministic approaches at a fraction of the computational cost. We also demonstrate that analytic tractography works on multiple diffusion sampling schemes, reconstruction method or parameters used to define paths. Open source software compatible with popular dMRI reconstruction software is provided.

**Keywords:** Diffusion MRI, white matter connectivity, analytic tractography

---

## 1. Introduction

The goal of structural connectivity research is to estimate the degree to which regions in the brain are connected by axonal projections, typically by making inferences on diffusion weighted MRI (dMRI) data. Any MRI-based method captures signal within a discrete set of voxels, meaning researchers are left to devise

---

*Email addresses:* matthew.cieslak@psych.ucsb.edu (Matthew Cieslak), tegan@cs.ucsb.edu (Tegan Brennan), meiring@pstat.ucsb.edu (Wendy Meiring), volz@psych.ucsb.edu (Lukas J. Volz), clint@ece.ucsb.edu (Clint Greene), asturias@psych.ucsb.edu (Alexander Asturias), suri@cs.ucsb.edu (Subhash Suri), grafton@psych.ucsb.edu (Scott T. Grafton)

a way to characterize projections spanning multiple voxels. Although dMRI analysis techniques differ in many technical aspects, they generally share two fundamental elements: quantitative estimates of fiber orientations within each voxel and an algorithm that utilizes these estimates to find sequences of voxels that are traversed by a putative white matter projection.

The first step of this paradigm most commonly involves fitting a tensor model to diffusion-weighted images (Basser et al., 2000), yielding a set of three directional eigenvectors. The principal eigenvector serves as the estimate of local fiber orientation. Other orientation models such as the ball-and-stick estimated by FSL's **BEDPOSTx** (Behrens et al., 2003), and the coefficients of spherical harmonic basis sets estimated via constrained spherical deconvolution (CSD) (Tournier et al., 2012) are more flexible than tensors. Deconvolution of the diffusion orientation distribution function (dODF) results in a “fiber ODF” (fODF or FOD) that is believed to be a more accurate representation of the true fiber orientations in each voxel because the dODF reflects fiber orientations convolved with an imaging-related point-spread function (Tournier et al., 2007; Descoteaux et al., 2009). Other approaches have foregone model estimation entirely and instead require a specific, sometimes quite lengthy, dMRI scanning protocol. For example, Diffusion Spectrum Imaging (DSI) can calculate a dODF analytically and has been shown to accurately represent multiple fiber orientations in a single voxel (Wedgeen et al., 2005, 2008). More recently, generalized q-sampling imaging (GQI) can analytically calculate dODFs across most q-space sampling schemes (Yeh et al., 2010). The dODFs produced by GQI and DSI can be further deconvolved or decomposed to produce fODFs. For simplicity we here refer to any function on the sphere with regularly-spaced angles as the domain and magnitudes as the range as an ODF, although tensors and fODF/FODs may not satisfy some other technical definitions of an ODF.

After one of the aforementioned methods has been used to quantify orientations in each voxel, the analyst can choose from a variety of algorithms that use this information to estimate fiber connectivity between distant voxels. Most of these tractography algorithms begin with some geometric assumptions about the paths of axons, namely that their shapes can be approximated by sequences of fixed-length segments that are joined at shallow angles. *Deterministic* tractography generates these sequences by selecting seed coordinates in relevant voxels and stepping along the directional maxima (i.e. principal eigenvectors or maxima of ODF lobes) until a stopping criterion is met. This criterion could be that the next voxel's peak direction(s) forms too steep an angle with the previous step or that the voxel has been deemed un-trackable due to low SNR or an anatomical mask. For example, consider two arbitrary regions in the brain  $a, b$  that are separated by multiple voxels. One could seed points throughout all of white matter and generate many deterministic paths (or streamlines) and count the number of streamlines that intersect both  $a$  and  $b$ . This method is simple, fast, and tends to produce biologically plausible trajectories. The method has some limitations, however. It is difficult to interpret streamline count (Jones et al., 2013) and any projection that fans within a voxel will not be accurately represented by the ODF peak alone.

On the other hand, the family of so-called *probabilistic* tractography algorithms use all available orientation information; be it a full tensor, dODF or fODF. This is accomplished by generating paths as sequences of geometrically-compatible steps that are sampled from a discretized version of the containing voxel's ODF as if it were a probability mass function (Koch et al., 2002). Revisiting the problem of estimating how connected region  $a$  is to region  $b$ , the probabilistic approach would mean seeding many points within  $a$  and growing paths by sampling the ODFs in each voxel. The number of paths that intersect  $b$  out of the total number of simulated paths serves as the estimate of connection probability. Many popular software implementations of this approach create a “connection density” (Behrens et al., 2007) or “track density” (Calamante et al., 2010) image that stores a count of the trajectories that passed through each voxel. This count is also referred to as the Probabilistic Index of Connectivity (PICO)(Parker & Alexander, 2003).

Consider the theoretical motivation behind probabilistic tractography. In order to connect regions  $a$  and  $b$  we must begin in a voxel in  $a$  and continue stepping across voxels until we reach a voxel in  $b$ . We are supposing that the ODF in each voxel reflects the proportion of myelinated axons that are parallel to each direction represented in the discretized ODF. These axons can exist anywhere in the voxel and can follow any geometrically-allowable trajectory within that voxel. As a physical object, the axon must enter the voxel from one of its 26 immediate neighbors and exit into another. If we select a voxel in  $a$  and seed a fixed number of points randomly within it. All these seeds will eventually exit into a neighboring voxel and continue to grow outwards. Only a fraction of these paths will go into each neighbor - and a smaller

fraction into the neighbor’s neighbors and so on. This has two important effects. The first is well-known: the probability of a trajectory reaching region  $b$  will decrease the more distant  $b$  is from  $a$ .

The second is more subtle and directly addressed by our proposed method. In reality, some fixed proportion of axonal fibers within the seed voxel project into each neighboring voxel. We define the proportion of axonal fibers connecting a voxel to one of its directly adjacent neighbors as the *ground-truth transition probability* of a fiber in the seed voxel continuing into this neighbor (if one were to randomly select an axon). Probabilistic tractography approximates this transition probability as the proportion of simulated paths that exit into each neighbor. The accuracy of this approximation depends directly on the number of seeds that are created within the voxel during probabilistic simulation. The fewer seeds generated, the more *simulation-related error* will impact the approximation. If seed points are only generated in voxels in region  $a$  this problem is compounded at each step. Fewer paths reach distant voxels, resulting in sparser sampling of the distant voxel ODFs and greater approximation error.

In theory we would need an infinite number of seeds in every voxel in order to avoid simulation-related error in connectivity estimations. Here we introduce a method that derives closed-form equations that directly calculate the voxel-to-voxel transition probabilities. We show experimentally that probabilistic simulations converge to our analytically calculated values as the number of simulated seeds increases. Our method precludes the need for any simulation at all, greatly decreasing the computational demand and bypassing the invariable exponential complexity that comes with tossing many coins at each step throughout the brain. This increase in efficiency does not come at the cost of any simplifying assumptions.

Analytically calculated voxel-to-voxel transition probabilities based on ODFs are useful for quantifying local white matter connectivity (between a voxel and its 26 immediate neighbors). However, additional tools are required to capture long-range connections. One already-established method for finding long-range projections based on local connectivity estimates can be called Voxel Graph tractography (Zalesky, 2008; Iturria-Medina et al., 2007, 2008). This approach treats each voxel in the brain as a node in a graph and the strength of its connectivity to its immediate neighbors as an edge weight. The use of analytically calculated voxel-to-voxel transition probabilities (i.e. using our closed-form solution) as edge weights in a Voxel Graph, defines what we call “Analytic Tractography.”

The use of analytic transition probabilities provides an improvement in accuracy, generality and speed over previously proposed Voxel Graph methods. The original method proposed by Zalesky (2008) required a tensor model, which will be deficient in regions of crossing, kissing or fanning fibers (Jones et al., 2013). Other approaches employ fast-marching methods to propagate paths across a Voxel Graph (Campbell et al., 2005; Iturria-Medina et al., 2007; Sotropoulos et al., 2010). These methods derived edge weights by constant solid angle integration of CSD fODFs in the direction of each neighboring voxel. This constant solid angle integration is based on the assumption that the ODF and axons are physically centered in the voxel, which represent an oversimplification.

We present four analyses that test the validity of our method and calculate its highest possible accuracy at capturing ground-truth transition probabilities when using to real dMRI data. First we show that given a set of ground-truth fibers from a software phantom, our method can calculate ground-truth transition probabilities based on fiber ODFs. Second, we use FiberFox to simulate dMRI from the software phantom and estimate transition probabilities based on dMRI-derived ODFs. Third, we empirically demonstrate that probabilistic tractography on ODFs from real datasets converge to the analytic values as the number of seeds increases. Finally, we show that Voxel Graph tractography based on analytic transition probabilities produces results comparable to those from other current methods at a fraction of the computational cost. Our demonstrations include many current methods for ODF estimation including HARDI, generalized q-sampling imaging, and diffusion spectrum imaging (DSI) both with and without ODF deconvolution.

### 1.1. ODFs to transition probabilities

We introduce two methods to calculate the probability that a white matter structure projects into an adjacent voxel. A closed-form expression for this transition probability is evaluated given a voxel’s ODF and a set of geometric constraints as inputs. Geometric constraints determine the allowable complexity of the white matter structure’s shape, preventing biologically implausible self-loops or spirals. Both methods hinge

on approximating white matter structure shape by discrete sequences of line segments called a “turning angle sequence”. Line segments are defined by a fixed length and orientation, with no two sequential segments connected at an angle greater than a user-specified fixed “maximum turning angle”.

Crucially, the directional magnitudes in an ODF do not specify the *location* of directed axon bundles within a voxel. Turning angle sequences accordingly do not have a fixed position within a voxel. For geometric constraints that prevent self-loops this ensures that the set of all possible turning angle sequences is finite. Transition probabilities can therefore be computed as sums over the set of turning angle sequences that could connect a voxel to an adjacent voxel, weighted by their probabilities. The proposed single-ODF and double-ODF methods diverge in how these probabilities are calculated.

For each voxel, the *single-ODF* method only considers ODF values from that voxel, assigning probabilities to turning angle sequences based on ODF magnitudes in the directions of the turning angle sequences. By contrast, the *double-ODF* method considers the ODFs of voxels on both sides of the source-destination transition, ensuring that there is evidence that the destination voxel “agrees” that a structure projects into it from the source voxel.

### 1.2. Fiber phantom analysis

To test the validity of the single-ODF and double-ODF methods, we used a set of artificial axonal fibers that were shaped to mimic the layout of a coronal slice through the human brain (Neher et al., 2014). This phantom provides an opportunity to calculate ground truth transition probabilities by constructing a voxel grid around the fibers and calculating the proportion of fibers that exit into each voxel’s neighbors. We perform two sets of validation tests. The first uses ground-truth fODFs, where the magnitude reflects the proportion of fibers parallel to each of a set of orientations, similar to those calculated in Track Orientation Density Imaging (Dhollander et al., 2014). With ground-truth fODFs as input we can compare the transition probabilities estimated by the single-ODF and double-ODF methods to actual ground-truth transition probabilities in the absence of imaging-dependent noise effects on fODF estimation. These effects are then introduced in the second set of tests, where the ground-truth fiber dataset is simulated in the FiberFox module of the MITK Diffusion software (Neher et al., 2014).

### 1.3. Transition probabilities in a voxel graph

While transition probabilities are specific to a voxel and its 26 neighbors, we can incorporate them into a Voxel Graph to trace fascicles across the brain. The Voxel Graph is a theoretically-sound but rarely-utilized technique described by Zalesky (2008) where white matter voxels are nodes connected to their immediate spatial neighbors. Edge weights are based on estimates that a white matter structure continues from one voxel into its neighbor (i.e. transition probabilities). By using the “logarithm trick,” weighting edges in the graph as the negative log of the transition probability, one can formulate brain connectivity as a shortest path problem (Zalesky, 2008). The probability that a voxel is connected to any other voxel is calculated as the product of the transition probabilities along the shortest path between the voxels. The shortest path is found efficiently using Dijkstra’s algorithm (Dijkstra, 1959). This forms the basis for estimating connectivity maps with analytic tractography.

To be of any practical use, analytic tractography should perform comparably to other state-of-the-art tractography methods. To this end, we built voxel graphs using the negative log of single-ODF and double-ODF transition probabilities from three datasets from the human connectome project (HCP, Van Essen & Ugurbil 2012). We built maps of shortest path probabilities to the rest of the brain to demonstrate that these highlight well-known projections. A source region in the cerebral peduncle should highlight the cortico-spinal tract and a source region in the corpus callosum should highlight inter-hemispheric U-fibers and lateral projections. These projections were reconstructed using both probabilistic (MRTRIX iFOD2 (Tournier et al., 2010), BEDPOSTx with probtrackx (Behrens et al., 2003, 2007), Bayesian tractography in CAMINO (Friman et al., 2006)) and deterministic tractography in DSI Studio (Yeh et al., 2013).

#### 1.4. Accompanying software

This paper is accompanied by open-source software that implements all the analyses presented here. The python package Mathematical solution for Inter-voxel Tract Transition Expectations requiring No Simulations (MITTENS) is available at [github.com/mattcieslak/MITTENS](https://github.com/mattcieslak/MITTENS). It can calculate transition probabilities and build and query voxel graphs. Although a number of groups have worked on the voxel graph method (Campbell et al., 2005; Hageman et al., 2009; Iturria-Medina et al., 2007; Sotropoulos et al., 2010), to our knowledge no software is publicly available that implements this method.

## 2. Methods

Analytic tractography uses ODF values and geometric constraints to directly calculate transition probabilities. We present two algorithms for defining the transition probabilities between adjacent voxels. Given a set of voxels,  $\mathbb{V}$ , and a discrete set of directions  $\Theta$ , the diffusion probability inside each voxel  $u \in \mathbb{V}$  in each direction  $\theta \in \Theta$  is given by  $\bar{p}_u(\theta)$  such that  $\sum_{\theta \in \Theta} \bar{p}_u(\theta) = 1$  (Wedge et al., 2005). The number of angles in  $\Theta$  is chosen by the analyst based on the angular resolution of their diffusion scans. While our methodology is applicable given any choice of symmetric  $\Theta$ , we chose the DSI Studio default of 642 evenly spaced directions for our presented experiments, resulting in an angular resolution of 8.09 degrees.

### 2.1. Turning angle sequences

Our approach introduces the concept of an abstract sequence of turning angles. A turning angle sequence  $\sigma = (\theta_0, \theta_1 \dots \theta_n)$  has no fixed start or end points in a voxel. It can be thought of as a template for a path, specifying the directions taken along the path but no spatial positioning. This abstract formulation nicely reflects that ODFs do not specify the within-voxel location of white matter structures (Kaden et al., 2007; Jones et al., 2013) unlike solid angle integration methods (Iturria-Medina et al., 2007; Sotropoulos et al., 2010) where the integration bounds are based on the ODF being centered in each voxel. Critically, the turning angle sequence abstraction allows us to analytically solve for transition probabilities between voxels.

Each of the uncountably infinite set of potential starting positions within the purple volume within voxel  $u$  of Figure 1(a) are equivalent in that they will result in a transition from voxel  $u$  to voxel  $v$  when following the specific turning angle sequence  $\sigma$ . If turning angle sequence  $\sigma$  begins anywhere else in voxel  $u$  it will not end with the last hop being from  $u$  into voxel  $v$ . The set of trajectories starting in the purple volume, following  $\sigma$  and ending in voxel  $v$  comprise one element in the finite set of equivalence classes that includes all possible multi-hop trajectories that start in voxel  $u$  and transition in the last hop into a neighboring voxel. The only necessary constraints are a maximum turning angle  $\theta_{max}$  and sufficiently large fixed step size.

Appropriate step size and maximum turning angle parameters ensure that each turning angle sequence eventually transitions into a neighboring voxel, thereby ensuring the set of equivalence classes is finite. These constraints also prevent biologically implausible fiber trajectories such as recurrent trajectories or loops within a voxel. These equivalence classes enable us to characterize all possible fiber trajectories within and between voxels directly.

### 2.2. Analytic Transition Probabilities

We quantify the probability of transitioning from voxel  $u$  into neighboring voxel  $v$  by summing over the probabilities of each turning angle sequence ( $\sigma$ ) that can end in  $v$ . Each turning angle sequence  $\sigma = (\theta_0, \theta_1 \dots \theta_n)$  has probability given by

$$P_u(\sigma) = \bar{p}_u(\theta_0) \times \bar{p}_u(\theta_1 | \theta_0) \times \dots \times \bar{p}_u(\theta_n | \theta_{n-1}) \quad (1)$$

i.e. each probability  $P_u(\sigma)$  is the product of the probabilities of taking each step in  $\sigma$ . The initial step  $\theta_0$  has a probability equal to the magnitude of the ODF of voxel  $u$  in direction  $\theta_0$ . The probabilities of subsequent hops are determined by both their angular similarity with the preceding turning angle and their magnitude in the ODF of voxel  $u$ . For example, higher angular similarity between consecutive turning angles could

increase the probability of  $\sigma$ . In our implementation we treat all geometrically compatible angles equally, and define the probability of taking direction  $\theta_i$  after taking  $\theta_{i-1}$  by

$$\bar{p}_u(\theta_i | \theta_{i-1}) = \bar{p}_u(\theta_i) \mathbf{1}(\theta_i, \theta_{i-1}) \left[ \sum_{\theta' \in \Theta} \bar{p}_u(\theta') \mathbf{1}(\theta', \theta_{i-1}) \right]^{-1} \quad (2)$$

where

$$\mathbf{1}(\theta, \theta') = \begin{cases} 1, & \text{if the angle between } \theta \text{ and } \theta' \text{ is less than } \theta_{max} \\ 0, & \text{otherwise.} \end{cases} \quad (3)$$

For a given  $\sigma$  and a neighboring target voxel  $v$ , we define  $\mathcal{V}(\sigma, v)$  as the volume given by integrating over all the potential starting points for  $\sigma$  in voxel  $u$  that result in the trajectory terminating in  $v$  without first stepping into any other voxel (see Figure 1 for an example). We implement a recursive algorithm to find the complete set of turning angle sequences  $\Sigma$  and their corresponding volumes,  $\mathcal{V}$ .

### 2.3. Recursive algorithm

Consider a starting voxel  $u$  and a neighboring target voxel  $v$ . A one-hop turning angle sequence from  $u$  to  $v$  is any  $\sigma = (\theta_*)$  for which there exists  $x, y$  such that  $x \in u, y \in v$ , and  $y = x + s\theta_*$  where  $s$  is the step size. We begin by finding all possible one-hop turning angle sequences that start in  $u$  and end in  $v$ . For each one-hop trajectory there is a volume  $\mathcal{V}((\theta_*), v)$  in  $u$  where the trajectory can begin such that it ends in  $v$ . Of note, this exhausts all possible one-hop trajectories from  $u$  to  $v$  for the given step size. All possible two-hop trajectories must be extensions of one-hop trajectories that start in  $u$ . In other words, two-hop turning angle sequences are defined *backwards*, by finding any possible hop within starting voxel  $u$  that ends in  $\mathcal{V}((\theta_*), v)$  for some one-hop turning angle sequence  $(\theta_*)$ . Further backwards hops are added until no more compatible hops within  $u$  can be found. In summary, this algorithm exhausts all possible turning angle sequences from  $u$  to  $v$  by first obtaining the critical  $\mathcal{V}((\theta_*), v)$  from which a single hop can terminate in target voxel  $v$  and then working backwards to identify all turning angle sequences and associated volumes. The resulting set of multi-hop turning angle sequences originating in starting voxel  $u$  is complete because all turning angle sequences of length  $n$  must be extensions of turning angle sequences of length  $n - 1$ .

For example, the trajectory  $\sigma$  illustrated in Figure 1 was obtained by first determining the volume (green cuboid) in  $u$  from which a hop in direction  $\theta_* = \theta_2$  terminated in target voxel  $v$ . Moving backwards, the next volume (orange cuboid) was then defined such that a hop in direction  $\theta_1$  terminated in the green cuboid. Repeating this step for  $\theta_0$  produced the purple cuboid, after which no further hops were possible within  $u$  for any  $\theta$  compatible with  $\theta_0$ .

Without biologically reasonable constraints on step size and maximum turning angle, one cannot guarantee that the above algorithm terminates. A large angular threshold or a small step size could result in infinite recursion. However such parameters will also lead to biologically implausible structures such as recurrent loops and spirals within a voxel. We use a fixed step size of  $\sqrt{3}/2$  voxels and a turning angle maximum of 35 degrees.

Importantly, the set of turning angle sequences is independent of empirical input data and only needs to be run once per step size and maximum turning angle. In practical terms, a set of turning angle sequences is calculated once (already included in the accompanying MITTENS software) and can subsequently be applied to any number of empirical datasets without the need for recalculations. In the following we define two complimentary methods that utilize the precalculated set of turning angle sequences to estimate transition probabilities on empirical data.

### 2.4. The single-ODF approach

The goal of the single-ODF approach is to define the transition probability between each voxel  $u$  and each of its adjacent voxels for empirical data. For a given voxel  $v$  from the 26 neighbors of  $u$  ( $\mathcal{N}(u)$ ), this

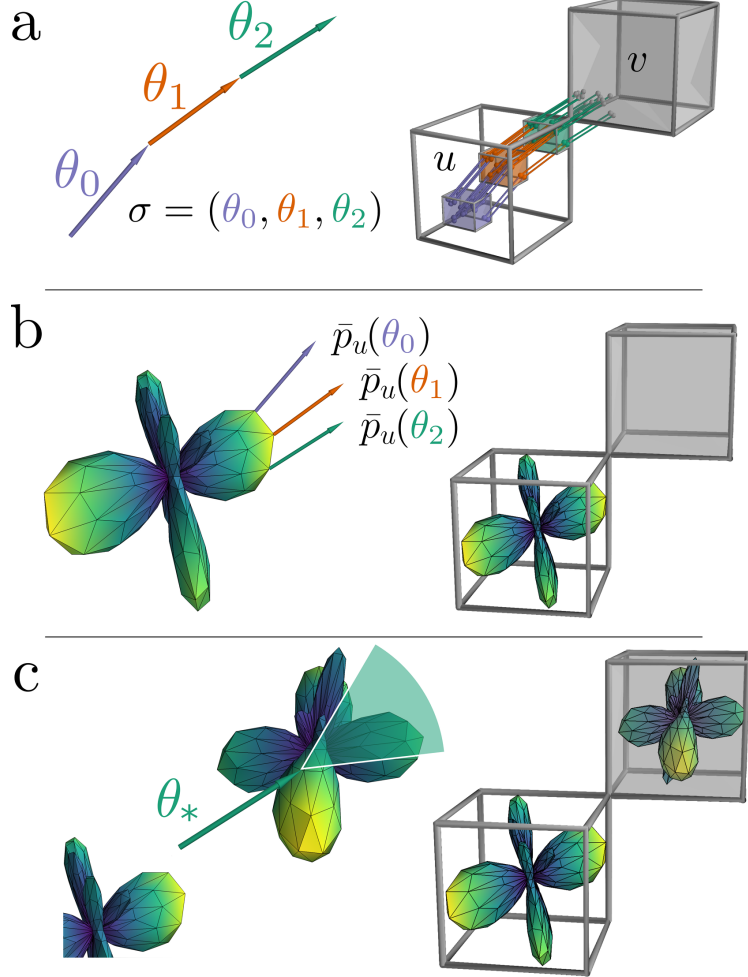


Figure 1: (a) On the left a turning angle sequence of three hops  $\sigma = (\theta_0, \theta_1, \theta_2)$  is shown. This sequence will form a trajectory from source voxel  $u$  to upper-right corner voxel  $v$  if it begins in the purple cubiod, which defines  $\mathcal{V}(\sigma, v)$ . A few random seeds were placed in  $\mathcal{V}(\sigma, v)$  and followed  $\sigma$  through space. All trajectories are seen to terminate in  $v$  as well as pass through the two intermediary volumes found by the recursive algorithm:  $\mathcal{V}((\theta_2), v)$  is green and  $\mathcal{V}((\theta_1, \theta_2), v)$  is orange. (b) A hypothetical ODF from source voxel  $u$  is plotted as a mesh, with the distance from the center corresponding to the probability associated with that direction. For single-ODF the probabilities corresponding to  $\theta_0, \theta_1, \theta_2$  are pulled directly from  $u$ 's ODF. (c) Transition probabilities calculated by double-ODF incorporate the ODF from voxel  $v$ . The directions in  $v$ 's ODF compatible with the direction taken into  $v$ ,  $\theta_* = \theta_2$  in this illustration, are included in the transition probability calculation.

transition probability from  $u$  to  $v$  is given by:

$$P(u \rightarrow v) = \sum_{\sigma \in \Sigma} P_u(\sigma) \mathcal{V}(\sigma, v) \quad (4)$$

where  $\Sigma$  is the finite set of turning angle sequences and  $\mathcal{V}(\sigma, v)$  is a proportion of the total voxel volume ( $\mathcal{V}(\sigma, v) \in [0, 1]$ ).

In this approach the transition probabilities depend only on the ODF of the starting voxel  $u$ . As illustrated in Figure 1b,  $P_u(\sigma)$  is completely determined by the ODF in  $u$ . The single-ODF transition probabilities from  $u$  to each of its 26 adjacent voxels are given by equation 4, concretized by the ODF of the starting voxel  $u$ . At a high level, the assumption that white matter structures influence the ODF motivates our use of the ODF to estimate the probabilities of existing white matter structures projecting through each

starting voxel into its neighbors. The single-ODF method elegantly transforms the starting voxel's ODF information into estimated transition probabilities.

### 2.5. The double-ODF approach

While the single-ODF approach produces a complete map of transition probabilities for the entire brain, it also introduces a potential problem. It computes a non-empty set of turning angle sequences connecting a voxel to all its neighbors that, on first glimpse implies that all voxels contain white matter structures connecting them to their neighbors. This is biologically implausible. To reduce this problem we introduce the double-ODF method, which simultaneously considers ODFs in both the starting and the target neighboring voxel. By penalizing conflicting directional diffusion information between ODFs of neighboring voxels, the transition probabilities are lower for neighbors that do not have compatible ODF values that provide evidence of white matter connections.

Our goal is to adjust transition probabilities in favor of trajectories likely to continue after exiting the starting voxel. To do so, the double-ODF method adjusts the probabilities of the turning angle sequences based on the ODF in target voxel  $v$ . Intuitively, the probability of a turning angle sequence exiting  $u$  at angle  $\theta_*$  will be increased if directions compatible with  $\theta_*$  have relatively high probability within  $v$ 's ODF. This is reflected mathematically through the introduction of a weighting term (5) that uses  $v$ 's ODF to calculate a similarity-based weight for a next step compatible with  $\sigma$  existing in  $v$ :

$$w(\sigma, v) = \sum_{\theta} \bar{p}_v(\theta) \mathbf{1}(\theta, \theta') \quad (5)$$

where  $\bar{p}_v(\theta)$  is the ODF value for  $\theta$  in  $v$ , and  $\mathbf{1}(\theta, \theta_*)$  is defined in equation 3. The summation is finite since  $\Theta$  is finite.

We use conditioning on  $(u \rightarrow \bullet)$  to denote the assumption that a “compatible” next hop exists in *at least one* neighbor of  $u$  after a turning angle sequence exits  $u$ . The double-ODF method computes the transition probabilities:

$$P(u \rightarrow v | u \rightarrow \bullet) = \frac{1}{\alpha} \sum_{\sigma \in \Sigma} P_u(\sigma) \mathcal{V}(\sigma, v) w(\sigma, v) \quad (6)$$

where

$$\alpha = P(u \rightarrow \bullet) = \sum_{v \in \mathcal{N}(u)} P(u \rightarrow \bullet | u \rightarrow v) P(u \rightarrow v) \quad (7)$$

We derive equation 6 using Bayes Theorem, under the assumption that the starting point for turning angle sequence  $\sigma$  (moving from  $u$  to  $v$ ) is uniformly distributed within  $\mathcal{V}(\sigma, v)$ :

$$\begin{aligned} & P(u \rightarrow v | u \rightarrow \bullet) \\ &= \frac{P(u \rightarrow \bullet | u \rightarrow v) P(u \rightarrow v)}{P(u \rightarrow \bullet)} \\ &= \frac{1}{\alpha} \sum_{\sigma \in \Sigma} P(u \rightarrow \bullet | \sigma \text{ and } u \rightarrow v) P(\sigma | u \rightarrow v) \mathcal{V}(\sigma, v) P(u \rightarrow v) \\ &= \frac{1}{\alpha} \sum_{\sigma \in \Sigma} w(\sigma, v) \mathcal{V}(\sigma, v) P(\sigma | u \rightarrow v) P(u \rightarrow v) \\ &= \frac{1}{\alpha} \sum_{\sigma \in \Sigma} w(\sigma, v) \mathcal{V}(\sigma, v) \frac{P_u(\sigma)}{P(u \rightarrow v)} P(u \rightarrow v) \\ &= \frac{1}{\alpha} \sum_{\sigma \in \Sigma} w(\sigma, v) \mathcal{V}(\sigma, v) P_u(\sigma) \end{aligned}$$

In contrast to the single-ODF version, the double-ODF approach is not purely local but depends on both the ODF in the current voxel and that in the target neighbor. As a result, the relative probability of a trajectory out of  $u$  into a neighbor increases for those neighbors that are more likely to contain a compatible trajectory with which to continue the path.

The double-ODF approach is comparable to the iFOD2 algorithm (Tournier et al., 2010) included in the MRTrix software package in that they both utilize ODFs (or FODs) in both the source and destination voxels while tracking. However, they differ in that iFOD2 re-combines (by interpolation) the source and destination FODs *during* tracking. As it is currently formulated, the iFOD2 approach does not have an analytic solution so must be simulated.

The double-ODF method is noteworthy in that it can result in a set of transition probabilities that are asymmetric about the center voxel. This could be a particularly useful feature in voxels where a y-split or fanning is not well-represented by a symmetric ODF. Recently methods for generating asymmetric ODFs based on surrounding voxels have been introduced (Reisert et al., 2012; Bastiani et al., 2017). The ability to capture asymmetric fiber populations within voxels was shown to reliably capture fiber patterns commonly seen histologically (Bastiani et al., 2017). These methods fit hyperparameters that introduce asymmetry to fODFs based on neighboring voxels. The double-ODF method does not require any specific ODF reconstruction technique and does not fit any parameters. There is also no theoretical barrier to using asymmetric ODFs as input to single-ODF or double-ODF equations.

## 2.6. Ground-truth validation test

The critical validity test for the single-ODF or double-ODF methods is whether they accurately calculate ground-truth transition probabilities when the underlying fibers are already known. This is made possible by the FiberFox (Neher et al., 2014) software included in the MITK Diffusion package. FiberFox takes as input a set of 3D “fibers” that represent myelinated axons. These fibers generate axon-like signal in simulated dMRI volumes, which can then be used to test whether a specific dMRI analysis pipeline is accurate in recreating the input fibers.

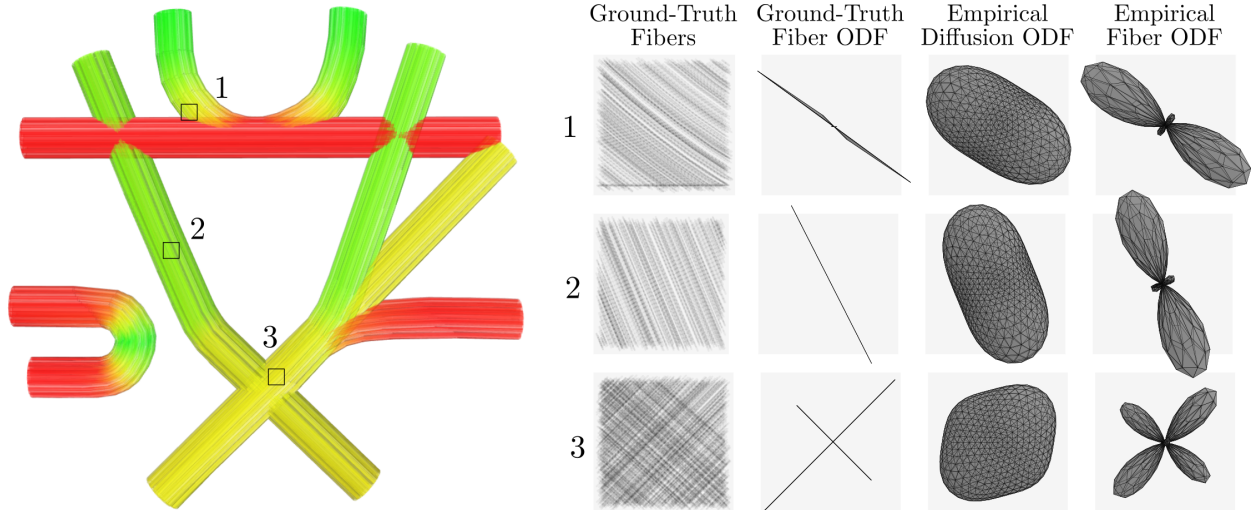


Figure 2: Left panel: The ground-truth fibers depicted as 3D streamlines. Three “voxels” were chosen to illustrate the differences between ODF types. Right panel: Each of the three illustrative voxels are displayed as rows of plots. The Ground-Truth Fibers column plots all ground-truth fiber segments contained within the voxel. The Ground-Truth Fiber ODF column shows the distribution of 0.1mm fiber segments along the canonical set of 642 directions. These same voxels were simulated in FiberFox using the HCP protocol. The GQI dODF and deconvolved fODF are shown in the final two columns.

We used the public release of the FiberCup fiber phantom from nitrc.org. The included fiber trajectories follow the shape of a well-known physical phantom (Poupon et al., 2010; Fillard et al., 2011) designed to mimic a coronal slice through the human brain (Figure 2, left). Synthetic voxel grids were created covering

the spatial extent of the fibers. At each voxel we calculated the ground-truth transition probabilities as the proportion of ground-truth fibers that intersect each of the 26 neighboring voxels. Within each voxel we also calculated a ground-truth fODF by breaking the contained fiber trajectories into 0.1mm segments. An angular histogram of these segments was calculated such that the histogram bins matched the angles represented in a 642-direction ODF. To match the symmetry in ODFs, counts in each bin were made symmetric by adding the counts along mirrored directions and normalized into probabilities. These ground-truth fODFs were used as input to the single-ODF and double-ODF equations and our closed form outputs were compared to the corresponding ground-truth transition probabilities.

No method currently exists to compute exact fODFs in living human brains, leaving us with imperfect estimations based on dMRI data. Indeed, we see in Figure 2 that the second column in the right panel depicts ground-truth fODFs that are mostly delta functions. This indicates no uncertainty or spread in the direction of fibers in a voxel, which would never be observed in dMRI-based ODFs. We therefore also used FiberFox (Neher et al., 2014) to simulate realistic dMRI volumes based on the ground-truth fibers sampled with the 270-direction multi-shell HARDI sequence from the human connectome project to create more realistic approximations of dMRI data, based on the ground-truth phantom structure. These simulated dMRI volumes were reconstructed in DSI Studio using GQI both with (Figure 2, fourth column) and without deconvolution (Figure 2, third column). The difference between analytic transition probabilities based on dMRI-derived ODFs provides a more realistic estimate of our method’s performance with empirical data.

### *2.7. Comparison of analytic and probabilistic transition probabilities*

Next we selected ODFs from two human dMRI datasets to empirically assess whether probabilistic simulations converge to the analytic transition probabilities as the number of seeds increases. We applied the single-ODF and double-ODF methods to two high-quality dMRI datasets. Both were reconstructed with multiple ODF reconstruction methods to evaluate the stability of calculated transition probabilities across a range of popular preprocessing pipelines.

The first data set was a multishell HARDI scan from a randomly selected subject from the human connectome project 900 subject release. The data were downloaded from the minimal-preprocessing repository (connectomedb.org). Diffusion scans were acquired at a spatial resolution  $1.25 \times 1.25 \times 1.25$  mm, with three q-shells at  $b = 1000, 2000$ , and  $3000$  s/mm $^2$ , 90 directions and 10 b0 images per shell. The minimal preprocessing pipeline included eddy current and motion correction, gradient unwarping, and geometric distortion correction using information from acquisitions in opposite phase-encoding directions (Glasser et al., 2013). These images were reconstructed in DSI Studio (Yeh et al., 2010) using GQI, with ODF deconvolution (regularization parameter set to 0.5), CSD (harmonic order=6, automated point spread function estimation, QBI regularization set to 0.006) and CSD with deconvolution (same parameters).

The second dataset included a total of 709 directions on a 7th-order Cartesian grid with a maximum b-value of 5000 s/mm $^2$  and voxel size of  $1.8 \times 1.8 \times 1.8$  mm. A total of 20 additional b0 images were acquired at regular intervals during the scanning. These images were extracted and used to perform motion correction. This dataset was reconstructed with both the original DSI technique (smoothing window length of 16) and GQI, both with and without ODF deconvolution (regularization parameter set to 0.5). No preprocessing was performed on the DSI data.

Four voxels were selected from each dataset to use for both probabilistic simulations and analytic transition probability calculation (Figure 3). One was located in the middle of the third ventricle (such that it contained no choroid plexus). This voxel contains freely diffusing cerebrospinal fluid and no white matter structures. Another voxel was chosen from the middle of the corpus callosum, which contains a fiber population projecting in a single direction. The third voxel came from a voxel in frontal lobe white matter that contains fibers from a local U-fiber and the superior longitudinal fasciculus. The fourth voxel contained fibers from the corticospinal tract, superior longitudinal fasciculus and a local U-fiber. ODFs in each of these four voxel types from both DSI and HCP datasets were estimated using all four reconstruction methods. To contrast the accuracy of our analytic, simulation-free method with the variability of transition probabilities estimated via simulations, we implemented the stochastic sampling algorithm of Koch et al. (2002) and calculated the distribution of transition probability estimates from 1000 runs of simulating  $10^3, 10^4, 10^5$ , and  $10^6$  seeds in each voxel. The means of these simulation-estimated transition probability distributions,

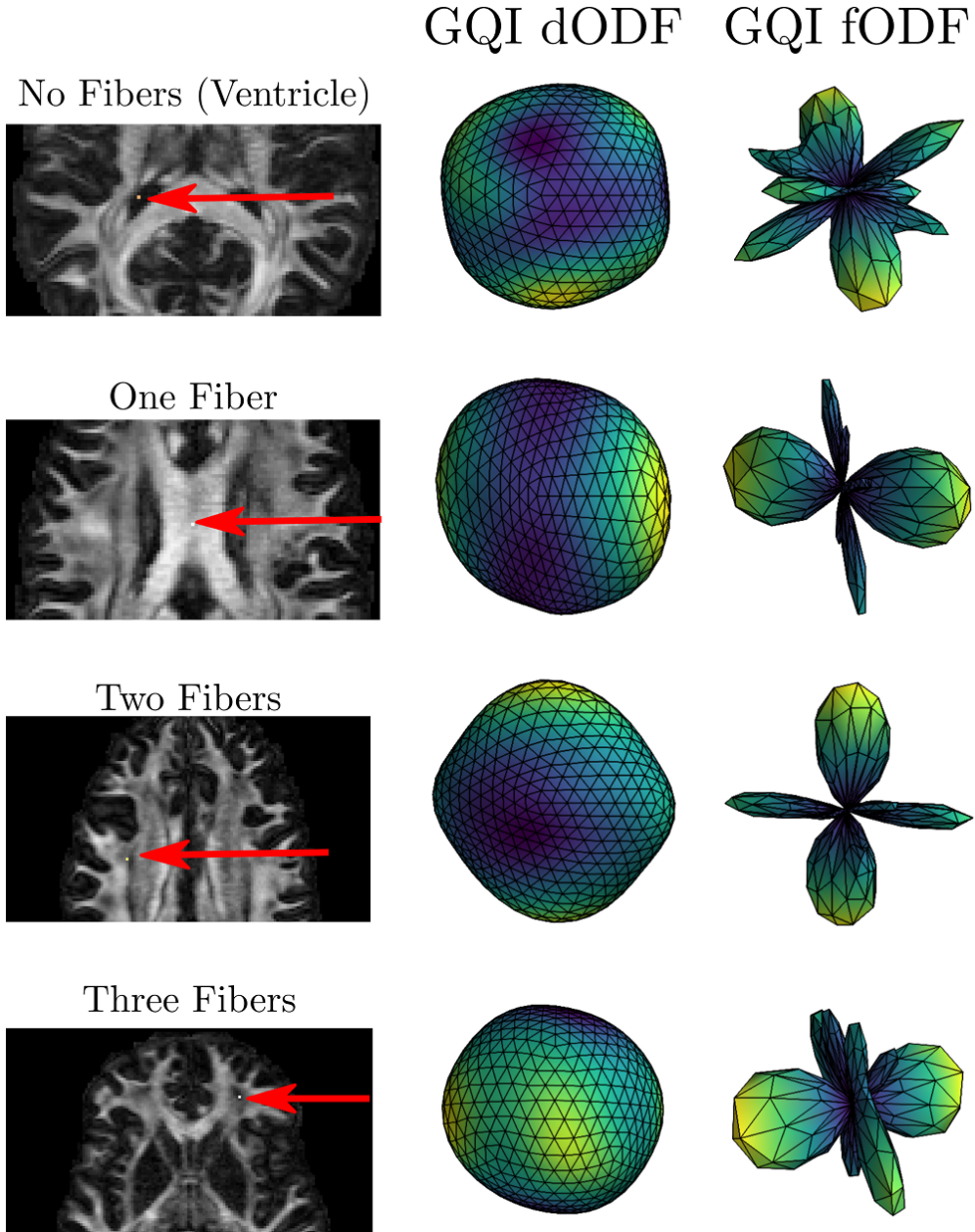


Figure 3: A single voxel was selected from four different regions of the brain, each with a different expected number of fiber populations. The source voxels are plotted in their containing axial slices (left column). The GQI diffusion ODF (dODF) from that voxel is shown in the middle column and the deconvolved GQI fiber ODF (fODF) in the right column.

based on real ODFs, were compared to the corresponding analytic transition probabilities calculated using the single-ODF method.

#### 2.8. Comparison of analytic voxel graphs to current tractography methods

Our goal here is to show that analytic transition probabilities can be used in a voxel graph to track known fascicles. We randomly selected three additional subjects from the HCP 900 subject release on which to run probabilistic, deterministic and analytic tractography. A multimodal symmetric group template (Avants

et al., 2007, 2010) was created with a 1.25mm isotropic voxel size from T1-weighted, T2-weighted and GFA volumes from a 28-subject age, gender and ethnicity stratified subset of the HCP 900 subject release. Our three selected subjects' T1-weighted, T2-weighted and GFA volumes were normalized to these templates using the SyN algorithm with cross correlation (Avants et al., 2008).

Source regions were drawn on the template image in the right cerebral peduncle and corpus callosum (Figure S3). The source regions were warped into each subject's native space for tractography. The voxelwise connectivity maps from each tractography method were warped into template space for comparison. The runtime of each tractography method was also recorded.

*Analytic tractography.* These were processed using GQI reconstruction with fiber deconvolution in DSI Studio. Single-ODF and double-ODF transition probabilities were calculated in MITTENS and voxel graphs were built using both formulations. Step size was  $s = \sqrt{3}/2$  and turning angle max was  $\theta_{max} = 35$  degrees. Adopting the approach taken by Zalesky (2008), we define the probability of a path as the product of the probability of each step along the path. By transforming each transition probability by the negative logarithm we ensure that the additive objective used in Dijkstra's algorithm is equivalent to maximizing the product of along-path probabilities<sup>1</sup>. Since these along-path probabilities are greatly attenuated with each additional step in the path, we quantify the strength of connection between two voxels as the mean probability along the connecting path. Finally, to generate the probability map, we assign to each voxel the maximum probability of any shortest path going through it.

It is worthwhile to note that this approach can potentially be improved by including curvature constraints during the path finding Sotropoulos et al. (2010). We use Dijkstra's algorithm directly without a curvature constraint to establish a lower bound of performance.

*Deterministic: DSI Studio.* The same GQI reconstructions used for analytic tractography were used for deterministic tractography in DSI Studio. We again used a step size of  $\sqrt{3}/2$ , a turning angle maximum of 35 degrees, a minimum length of 10mm, maximum length of 140mm, and a QA threshold automatically determined by DSI Studio. All white matter voxels were seeded and tracking was performed until  $10^6$  streamlines intersecting the source region were reconstructed. This set of streamlines was used to create a track density image that was used as the summary output for this method.

*Probabilistic: MRTRIX.* These same preprocessed datasets were processed in MRTRIX3. Multi-shell multi-tissue constrained spherical deconvolution was used to reconstruct fODFs in each voxel,  $l_{max} = 8$  (Jeurissen et al., 2014). Probabilistic tractography was run using the iFOD2 algorithm with anatomically constrained tractography enabled and the following parameters: step size of 0.5mm, maximum length of 250mm, maximum angle between steps 80 degrees, 10,000 randomly placed seeds per voxel. The output tracking was cropped at the GM-WM interface and converted into a track density image for comparison to other methods.

The tracking output was summarized as a track density image, which we used for comparison to other methods.

*Probabilistic: CAMINO.* The datasets were processed in CAMINO so that Bayesian probabilistic tractography could be performed (Friman et al., 2006). We followed the recommended steps on the CAMINO website for processing HCP data. Diffusion weighted images where  $b > 1000$  were discarded before passing data to CAMINO's `track` program. The Bayes Dirac model was used with a curvature threshold of 70 degrees over 5mm and the reduced set of 1082 directions for 1000 iterations. Tracking results were here also summarized as track density images.

*Probabilistic: probtrackx.* The results of processing these same subjects with BEDPOSTx were downloaded from the HCP database. These were further processed with probtrackx2 using the parameters recommended for HCP analysis in the FSL mailing list. Specifically, loop checking was enabled, distance correction was

---

<sup>1</sup>MITTENS supports other metrics for finding paths between voxels such as the “bottleneck” metric used by Iturria-Medina et al. 2007.

applied, default curvature threshold of 0.2, default volume fraction of 0.01, 2000 step maximum, 10,000 samples, step size of 0.5mm, voxel center seeding, and no distance threshold. The corrected output path distribution was used for comparison to other methods.

### 3. Results

#### 3.1. Analytic transition probabilities vs ground-truth transition probabilities

Figure 4 shows the empirical cumulative distribution function (CDF) of absolute differences between analytic transition probabilities and ground-truth transition probabilities for single-ODF and double-ODF calculations based on each of three types of input ODF values (6 curves per panel), for each of three voxel resolutions (three panels). The double-ODF method was more accurate than single-ODF overall.

At first glance these CDFs seem to indicate that there is considerable error – particularly for single-ODF transition probabilities. It is important to note that these are CDFs for the absolute value of the error. For double-ODF the least accurate condition was 1.25mm voxels with a mean error of  $10^{-20} \pm 0.04$  standard deviation. For single-ODF the least accurate condition was 3mm dODF with a mean error of  $5.4^{-11} \pm 0.08$  standard deviation. Recall that errors can be introduced by the forced-symmetry or the discretized angles in the ground-truth fODFs. The same step size and maximum turning angle were used for each voxel size, which means that different across-voxel fiber trajectories were possible at each resolution. This likely also contributes to error rate.

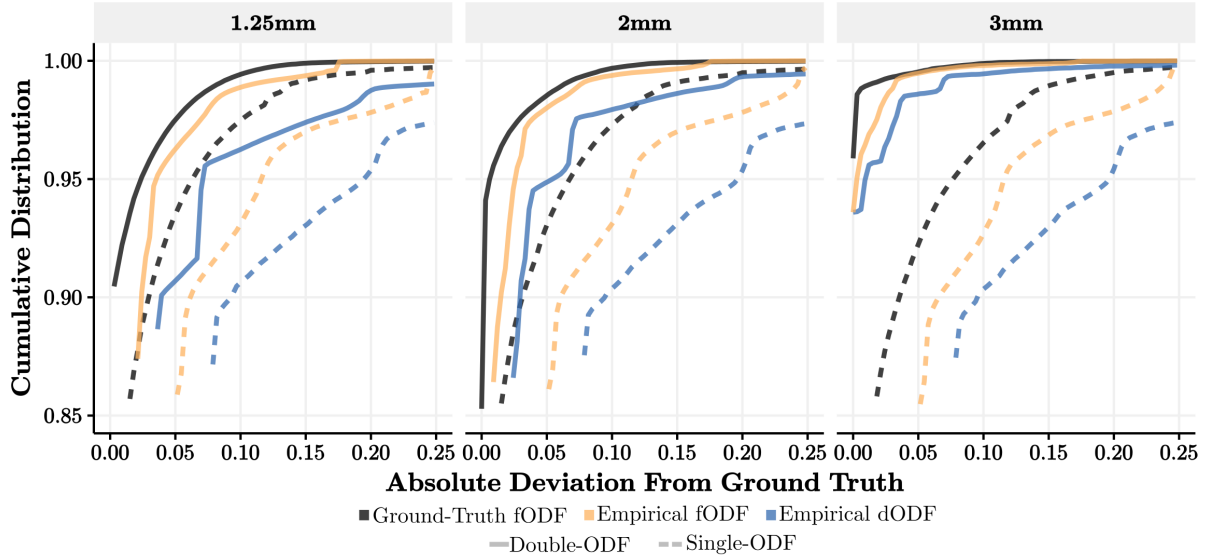


Figure 4: This figure plots the error CDF of analytic transition probabilities with three different types of ODFs as input. The results for ground-truth fODFs are plotted in black, the others were ODFs reconstructed from FiberFox simulated dMRI: GQI dODFs are plotted in blue and deconvolved GQI fODFs in yellow. The error CDFs for double-ODF transition probabilities are solid lines and single-ODF are dashed. Only voxels with 26 neighbors inside the fiber phantom were included. The lines begin at the percentile of the first non-zero error observed. Results for 1.25mm, 2mm and 3mm voxels are presented in separate panels.

Critically, the face-validity check (using ground-truth fODFs) of the analytic transition probabilities against ground-truth transition probabilities shows that the errors at the 95th percentiles are quite low. For the double-ODF method the errors at the 95th percentile were all 0 at 3mm,  $\leq 0.006$  at 2mm, and  $\leq 0.02$  at 1.25mm. For the single-ODF method the errors at the 95th percentile were  $\leq 0.08$  at 3mm,  $\leq 0.07$  at 2mm, and  $\leq 0.06$  at 1.25mm. The double-ODF method is notably more successful at recovering the true transition probabilities.

### 3.2. Probabilistic transition probabilities converge to analytic values

Figure 5 empirically demonstrates that probabilistic simulation-generated transition probability estimates converge to the analytic transition probabilities when operating on the same ODF data. The differences between the simulation distribution means and analytic transition probabilities were less than  $10^{-10}$  when  $10^4$  or more seeds were simulated. This is notable since  $10^{-10}$  is smaller than IEEE float32 precision (which is accurate up to  $10^{-6}$ ) but still representable by the float64 datatype used during the simulation (which can represent up to  $10^{-15}$ ).

Note that the variability of the stochastic simulation estimates increases when fewer seeds are sampled. For example, simulation-related error distributions plotted in Figure 5 reflect that the estimates from  $10^6$  seeds have substantially lower error ( $\pm 10^{-5}$ ) compared to those using  $10^4$  seeds ( $\pm 10^{-4}$ ).

Analytic transition probabilities are accurate regardless of how the data were acquired (DSI or multishell HARDI), how the ODFs were reconstructed (GQI, DSI and CSD), whether or not ODF deconvolution was applied and regardless of the complexity of the tissue contained in the voxel. The results for the 7th-order Cartesian grid q-space sampling (i.e. a high-quality DSI scan) are presented in figure S2.

Notably, in both the HCP and DSI cases the simulation means begin to converge to the analytic solution when  $10^4$  or more seeds per voxel are simulated. However even  $10^4$  seeds do not provide transition probability estimates that are free from simulation error. The simulation-related error in transition probabilities decreases by a factor of 10 for each corresponding increase by a factor of 10 in the number of simulated seeds, whereas our analytic results are free of simulation-related error.

### 3.3. Analytic voxel graph tractography is fast and comparable to other methods

Following the approach of Sotropoulos et al. (2010) we extracted the connectivity scores weights from all the nonzero-scored voxels output from each method. In Figure 6 we plot 3D surfaces of the voxels with scores in the top 5% and 2% of each method's results. These are displayed for the cerebral peduncle source region in Figure 6 (left) and for the corpus callosum region (right). These surfaces are displayed axially in Figure S4.

Each method presented in Figure 6 behaves consistently across all three subjects. All methods are able to find a path from the peduncle to motor cortex, but the spatial extent of this connection varies considerably. Deterministic tractography is much more sparse than the other methods, but this may be due to its conversion to a track density image (TDI). Most of the million streamlines follow the same paths, which results in little variability in the TDI, which in turn arbitrarily shrinks the spatial extent when thresholding based on percentiles.

We compared spatial similarity of each method's output by calculating Spearman's  $\rho$  between the different methods<sup>2</sup>. These comparisons included all white matter voxels ( $\approx 900,000$ ) per subject. Table 1 lists the within-subject  $\rho$  values across the three subjects. The double-ODF and iFOD2 results are an interesting comparison since they both "peek" into neighboring ODFs at some point in processing. Double-ODF incorporates the neighbor voxel's ODF directly into the transition probability calculation while iFOD2 performs a weighted average of the fODFs at each step of the probabilistic simulations. We observed that iFOD2 produced the most similar results to analytic tractography with  $\rho$  up to 0.71 for the corpus callosum ROI and up to 0.76 for the cerebral peduncle ROI. In both cases these are the highest similarities observed across methodologies.

There is a large difference between analytic tracking and the probabilistic methods in computation time. On average, probtrackx took 38 minutes per region, Bayes Dirac took 38 minutes and iFOD took an estimated 5 hours. Calculating a whole-brain shortest path map after calculating analytic transition probabilities took an average of only 0.64 seconds. A single query from a source region results in a probability value in each voxel, so constructing a region-to-region connectivity matrix would take about 0.64 seconds per region in the atlas using voxel-graph methods with analytic transition probabilities as edge weights.

<sup>2</sup>Spearman's  $\rho$  was chosen instead of Pearson's  $r$  because the connection weights estimated by probabilistic methods are approximately exponentially distributed while analytic connection weights are approximately normally distributed. Therefore rank-based Spearman's  $\rho$  was used.

Table 1: Connectivity map similarity for 3 HCP subjects

	Method	Deterministic	MRTRIX iFOD2	Bayesian DT	Single-ODF	Double-ODF
Corpus Callosum	PROBTRACKx	27, 24, 23	62, 61, 63	49, 42, 45	51, 51, 53	51, 51, 53
	Deterministic		24, 24, 21	28, 29, 3	16, 15, 16	15, 14, 16
	MRTRIX iFOD2			37, 33, 34	64, 65, 71	64, 65, 71
	Bayesian DT				26, 24, 27	27, 24, 28
Single-ODF	Method	Deterministic	MRTRIX iFOD2	Bayesian DT	Single-ODF	Double-ODF
	PROBTRACKx	28, 28, 28	62, 62, 63	56, 55, 53	48, 47, 47	49, 48, 49
	Deterministic		28, 30, 28	31, 31, 33	22, 23, 21	23, 23, 22
	MRTRIX iFOD2			32, 33, 32	77, 75, 74	78, 76, 76
Cerebral Peduncle	Bayesian DT				22, 19, 21	22, 20, 21
	Single-ODF					98, 98, 98

Spearman's  $\rho$  calculated pairwise on connectivity maps from probabilistic, deterministic and analytic tractography methods. Values are presented are multiplied by 100 for easier reading.

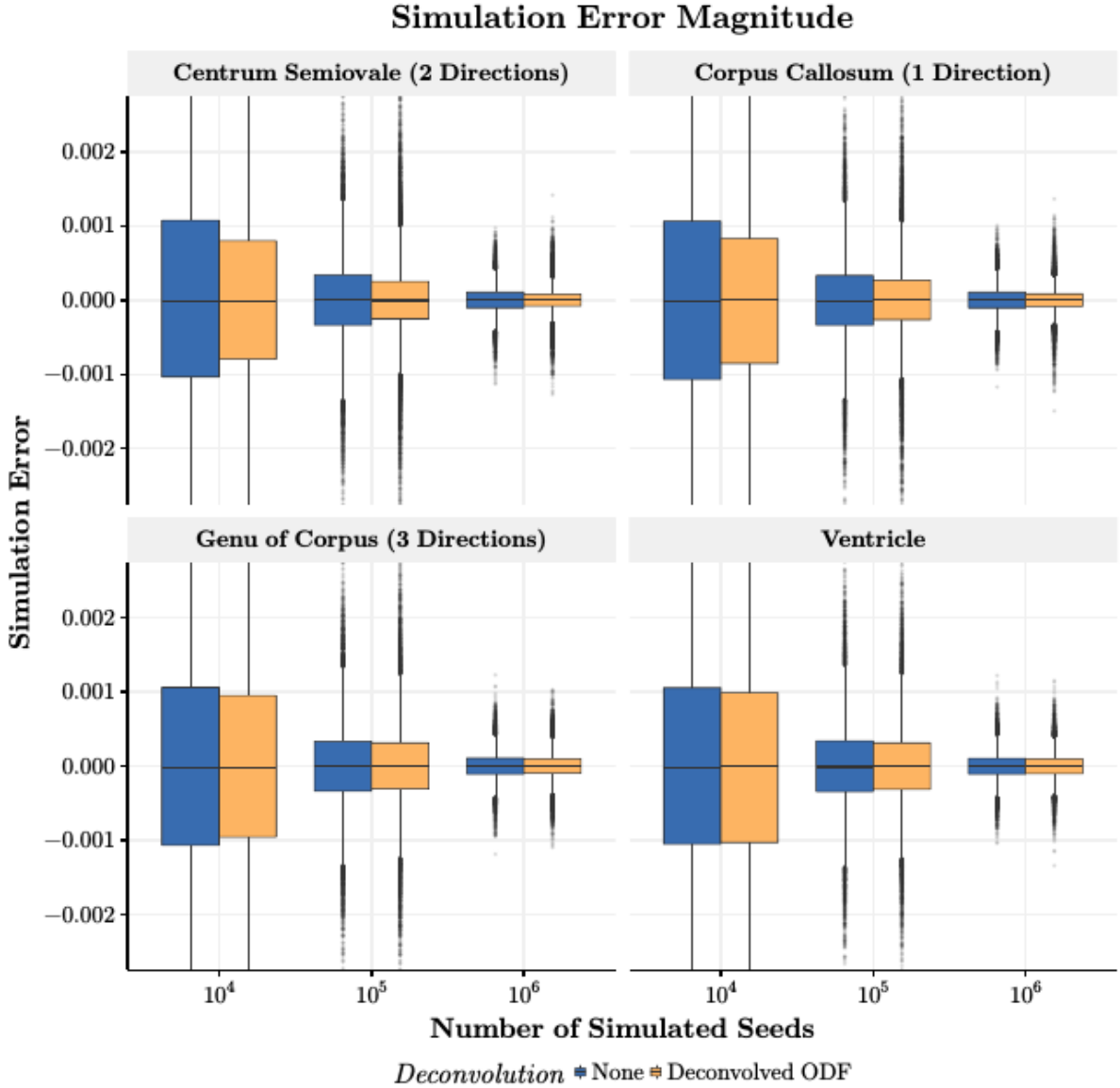


Figure 5: Distributions of the magnitude of simulation-related error as a function of the number of simulated seeds. Depicted in the boxplots are all differences between the simulation-based transition probability estimation and the analytic transition probability using the single-ODF method. Each panel depicts a voxel from Figure 3. ODFs used here came from an HCP HARDI dataset reconstructed using GQI. Blue boxes display the dODF-based and yellow display the fODF-based error distributions.

#### 4. Discussion

The analytic tractography framework provides fast, theoretically grounded tools for quantifying white matter structure through dMRI data. Closed-form solutions for two types of transition probabilities provide precision that simulation-based methods can only approximate. Moreover, by avoiding simulation, the accuracy of analytic methods does not depend on the number of simulations run. Furthermore, the analytic solutions can be calculated for any q-space sampling scheme or ODF reconstruction method. This gener-

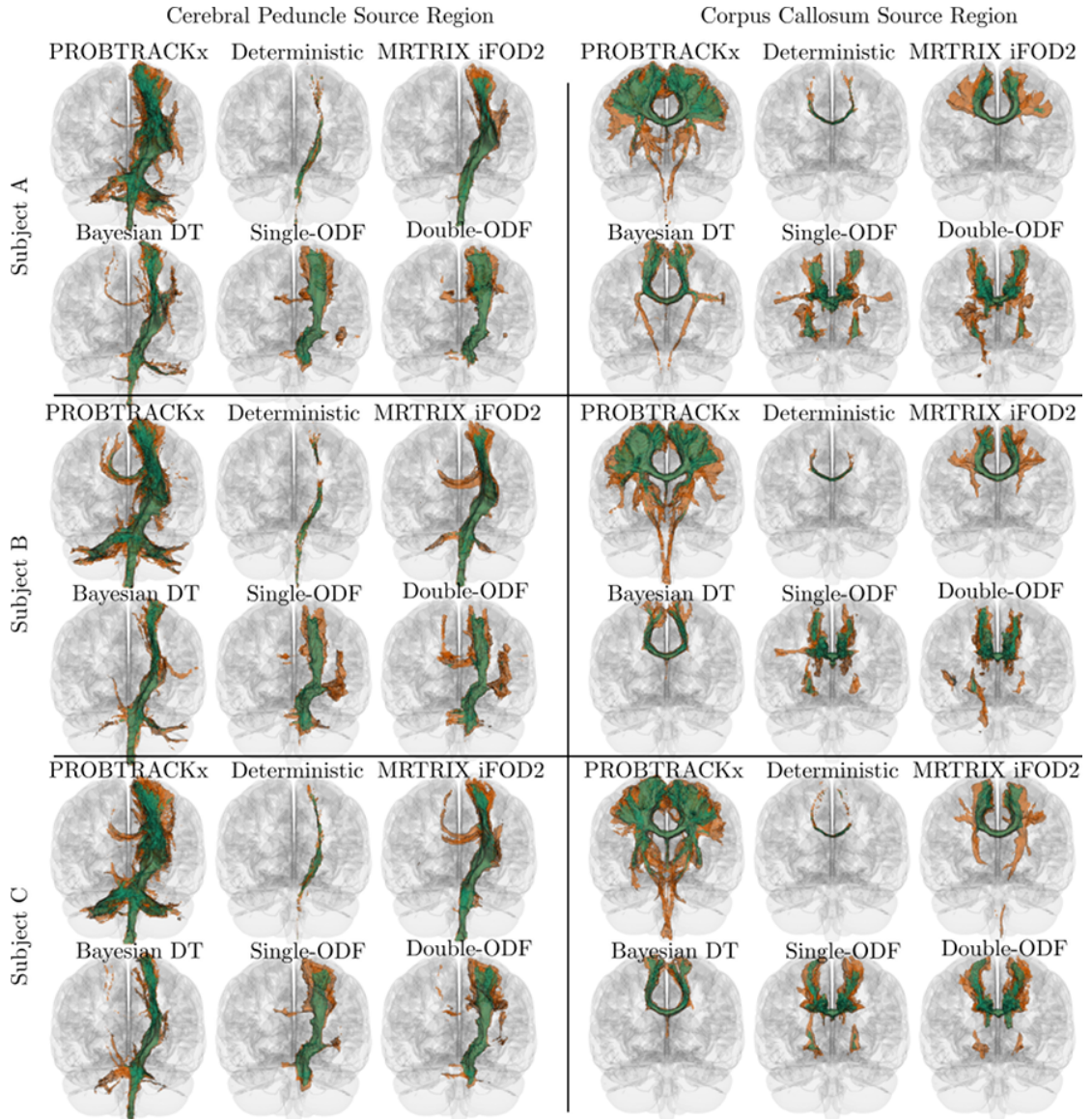


Figure 6: Tractography results from three HCP subjects. Voxels within the top 5% of connectivity scores are enclosed in an orange surface and the top 2% are enclosed in a green surface. The tractography method used to generate the map is listed above the brain images. Images in the left panels are the result of tracking from the cerebral peduncle ROI, and the right result from tracking from the corpus callosum ROI.

ability frees the experimenter from an additional set of simulation-related parameters in an already complex processing pipeline. The efficiency and precision of calculation enables researchers to rapidly explore the effects of choices in other parameter spaces such as ODF reconstruction and deconvolution.

Although the low computational demands of analytic tractography are a desirable feature, it can rightly be argued that the probabilistic simulations run by most current software can also be run on GPUs at comparable speeds (Hernández et al., 2013). We emphasize that even though GPUs can simulate seeds quickly, they will still be simulating a finite number of seeds in a subset of voxels – leading to simulation-related error. We have demonstrated that simulating  $10^6$  seeds per voxel will produce simulation-related errors on the order of  $10^{-4}$ , but this error rate only applies to voxels explicitly included in a seed region. Voxels external to the seed region will be sampled by exponentially fewer seeds and will have a corresponding

increase in error.

We demonstrate empirically that the result of probabilistic tractography converges to the analytic solution as the number of seeds increases. This result should be viewed in the context of our comparison of the single-ODF method to ground-truth transition probabilities. Transition probabilities simulated on one single, symmetric ODF at a time were markedly less accurate than asymmetric transition probabilities calculated by the double-ODF method that incorporates multiple ODFs. This performance drop was observed in noise-free simulated dMRI, meaning that more severe drops may be observed on noisy real dMRI data. We see this as compelling motivation to adopt asymmetric ODF-capable methods such those proposed by Reisert et al. (2012) and Bastiani et al. (2017).

The directed voxel graph built from transition probabilities opens up new possibilities in brain network analysis. Current network science methods primarily model data that are described at the anatomic resolution of large cortical regions. They typically make use of tractography to weight edges. These weights are sensitive to a large number of tractography reconstruction parameters (Bassett et al., 2011). In contrast, our voxel graph application is insensitive to these reconstruction choices and will instead efficiently evaluate all possible tractograms – providing a probability for each path. Furthermore, these path probabilities are free of simulation-based errors that accumulate at each step in probabilistic tractography. The tracking method presented here does have the previously noted distance bias (Iturria-Medina et al., 2011), but this bias manifests as a regression-to-the-mean instead of an exponential decay. Future work will investigate more robust methods for calculating path probabilities.

Voxel graphs are computationally efficient. The graph only needs to be constructed once for the whole brain, after which it can be queried from any arbitrary location. Fortunately, finding the shortest, or even the top  $k$  shortest paths in a graph is a computationally tractable problem. An arsenal of efficient computational approaches do this well; a number of efficient algorithms are known whose running time is essentially linear in the size of the voxel graph (Dijkstra, 1959). We observed up to a 2,812,500% improvement in processing time over comparable CPU-based probabilistic tractography methods. Our method should accelerate the evolution of these approaches.

We have not addressed the issue of how to construct region-to-region structural connectivity matrices here. There are already numerous methods for using Voxel Graphs to estimate the connection strength between regions. These include Anatomical Connection Strength, Anatomical Connection Density, and Anatomical Connection Probability as proposed by Iturria-Medina et al. (2007) or capacity as proposed by Zalesky & Fornito (2009). Sotropoulos et al. (2010) also propose a number of methods. Future work will investigate structural connectivity matrices using Voxel Graphs.

A unique avenue of connectivity quantification is possible with voxel graphs. Recent work shows that specific regions in deep white matter are prone to a high rate of false connections in current tractography methods (Maier-Hein et al., 2016). We could potentially identify these regions, as we can now compute centrality measures in individual voxels. In fact, network measures that are commonly calculated for entire brain regions can now be calculated voxelwise in all of white matter. While we demonstrate shortest path queries on voxel graphs, this is only one example of the many opportunities to pursue novel connectivity metrics. Our software is easy to install and use, providing a means for the community to do so.

Future work should address the problem of large-scale geometric constraints on shortest path trajectories. Another direction for future research would be an exhaustive test of the step size and turning angle max parameters over a range of commonly-used voxel sizes. Using a more realistic fiber phantom such as the one introduced by Maier-Hein et al. (2016) as ground-truth and calculating error CDFs across a grid of step size and angle max parameters would allow for fine-tuning these choices based on voxel sizes that could be useful for other tractography methods as well. Once tuned, this method may be useful for clinical applications that are typically approached with tractography-based methods.

## Acknowledgements

This research was supported by a Head Health Challenge grant from General-Electric and the National Football League and Institute for Collaborative Biotechnologies through grant W911NF-09-0001 from the U.S. Army Research Office.

## References

### References

- Avants, B., Duda, J. T., Zhang, H., & Gee, J. C. (2007). Multivariate Normalization with Symmetric Diffeomorphisms for Multivariate Studies. In *Medical Image Computing and Computer-Assisted Intervention – MICCAI 2007* (pp. 359–366). Berlin, Heidelberg: Springer Berlin Heidelberg.
- Avants, B. B., Epstein, C. L., Grossman, M., & Gee, J. C. (2008). Symmetric diffeomorphic image registration with cross-correlation: evaluating automated labeling of elderly and neurodegenerative brain. *Medical image analysis*, *12*, 26–41.
- Avants, B. B., Yushkevich, P., Pluta, J., Minkoff, D., Korczykowski, M., Detre, J., & Gee, J. C. (2010). The optimal template effect in hippocampus studies of diseased populations. *Neuroimage*, *49*, 2457–2466.
- Basser, P., Pajevic, S., Pierpaoli, C., Duda, J., & Aldroubi, A. (2000). In vivo fiber tractography using DT-MRI data. *Magnetic Resonance in Medicine*, *44*, 625–632.
- Bassett, D. S., Brown, J. A., Deshpande, V., Carlson, J. M., & Grafton, S. T. (2011). Conserved and variable architecture of human white matter connectivity. *Neuroimage*, *54*, 1262–1279.
- Bastiani, M., Cottaar, M., Dikranian, K., Ghosh, A., Zhang, H., Alexander, D. C., Behrens, T. E., Jbabdi, S., & Sotiroopoulos, S. N. (2017). Improved tractography using asymmetric fibre orientation distributions. *NeuroImage*, *158*, 205–218.
- Behrens, T. E., Berg, H. J., Jbabdi, S., Rushworth, M., & Woolrich, M. (2007). Probabilistic diffusion tractography with multiple fibre orientations: What can we gain? *Neuroimage*, *34*, 144–155.
- Behrens, T. E., Woolrich, M., Jenkinson, M., Johansen-Berg, H., Nunes, R., Clare, S., Matthews, P., Brady, J. M., & Smith, S. M. (2003). Characterization and propagation of uncertainty in diffusion-weighted MR imaging. *Magnetic resonance in medicine*, *50*, 1077–1088.
- Calamante, F., Tournier, J. D., Jackson, G. D., & Connelly, A. (2010). Track-density imaging (TDI): Super-resolution white matter imaging using whole-brain track-density mapping. *NeuroImage*, *53*, 1233–1243.
- Campbell, J. S. W., Siddiqi, K., Rymar, V. V., Sadikot, A. F., & Pike, G. B. (2005). Flow-based fiber tracking with diffusion tensor and q-ball data: Validation and comparison to principal diffusion direction techniques. *NeuroImage*, *27*, 725–736. doi:10.1016/j.neuroimage.2005.05.014.
- Descoteaux, M., Deriche, R., Knosche, T. R., & Anwander, A. (2009). Deterministic and probabilistic tractography based on complex fibre orientation distributions. *IEEE transactions on medical imaging*, *28*, 269–286.
- Dhollander, T., Emsell, L., Van Hecke, W., Maes, F., Sunaert, S., & Suetens, P. (2014). Track orientation density imaging (tod) and track orientation distribution (tod) based tractography. *NeuroImage*, *94*, 312–336.
- Dijkstra, E. W. (1959). A note on two problems in connexion with graphs. *Numerische mathematik*, *1*, 269–271.
- Fillard, P., Descoteaux, M., Goh, A., Gouttard, S., Jeurissen, B., Malcolm, J., Ramirez-Manzanares, A., Reisert, M., Sakaie, K., Tensaouti, F. et al. (2011). Quantitative evaluation of 10 tractography algorithms on a realistic diffusion mr phantom. *NeuroImage*, *56*, 220–234.
- Friman, O., Farneback, G., & Westin, C.-F. (2006). A Bayesian approach for stochastic white matter tractography. *IEEE transactions on medical imaging*, *25*, 965–978.
- Garyfallidis, E., Brett, M., Amirbekian, B., Rokem, A., van der Walt, S., Descoteaux, M., & Nimmo-Smith, I. (2014). Dipy, a library for the analysis of diffusion MRI data. *Frontiers in neuroinformatics*, *8*, 8.
- Glasser, M. F., Sotiroopoulos, S. N., Wilson, J. A., Coalson, T. S., Fischl, B., Andersson, J. L., Xu, J., Jbabdi, S., Webster, M., Polimeni, J. R. et al. (2013). The minimal preprocessing pipelines for the Human Connectome Project. *Neuroimage*, *80*, 105–124.
- Hageman, N., Toga, A., Narr, K., & Shattuck, D. (2009). A diffusion tensor imaging tractography algorithm based on Navier-Stokes fluid mechanics. *Medical Imaging, IEEE Transactions on*, *28*, 348–360.
- Hernández, M., Guerrero, G. D., Cecilia, J. M., García, J. M., Inuggi, A., Jbabdi, S., Behrens, T. E., & Sotiroopoulos, S. N. (2013). Accelerating fibre orientation estimation from diffusion weighted magnetic resonance imaging using GPUs. *PLoS One*, *8*, e61892.
- Iturria-Medina, Y., Canales-Rodríguez, E., Melie-García, L., Valdes-Hernandez, P., Martínez-Montes, E., Alemán-Gómez, Y., & Sánchez-Bornot, J. (2007). Characterizing brain anatomical connections using diffusion weighted MRI and graph theory. *Neuroimage*, *36*, 645–660.
- Iturria-Medina, Y., Pérez Fernández, A., Morris, D. M., Canales-Rodríguez, E. J., Haroon, H. A., García Pentón, L., Augath, M., Galán García, L., Logothetis, N., Parker, G. J. M., & Melie-García, L. (2011). Brain hemispheric structural efficiency and interconnectivity rightward asymmetry in human and nonhuman primates. *Cerebral cortex (New York, N.Y. : 1991)*, *21*, 56–67.
- Iturria-Medina, Y., Sotero, R. C., Canales-Rodríguez, E. J., Alemán-Gómez, Y., & Melie-García, L. (2008). Studying the human brain anatomical network via diffusion-weighted mri and graph theory. *Neuroimage*, *40*, 1064–1076.
- Jeurissen, B., Tournier, J.-D., Dhollander, T., Connelly, A., & Sijbers, J. (2014). Multi-tissue constrained spherical deconvolution for improved analysis of multi-shell diffusion MRI data. *NeuroImage*, *103*, 411–426.
- Jones, D. K., Knösche, T. R., & Turner, R. (2013). White matter integrity, fiber count, and other fallacies: The do's and don'ts of diffusion MRI. *NeuroImage*, *73*, 239–254.
- Kaden, E., Knösche, T. R., & Anwander, A. (2007). Parametric spherical deconvolution: Inferring anatomical connectivity using diffusion MR imaging. *NeuroImage*, *37*, 474–488.
- Koch, J., Staudt, C. L., Vogel, M., & Meyerhenke, H. (2016). An empirical comparison of Big Graph frameworks in the context of network analysis. *Social Network Analysis and Mining*, *6*, 84.

- Koch, M. A., Norris, D. G., & Hund-Georgiadis, M. (2002). An Investigation of Functional and Anatomical Connectivity Using Magnetic Resonance Imaging. *NeuroImage*, *16*, 241–250. doi:10.1006/nimg.2001.1052.
- Maier-Hein, K., Neher, P., Houde, J.-C., Cote, M.-A., Garyfallidis, E., Zhong, J., Chamberland, M., Yeh, F.-C., Lin, Y. C., Ji, Q. et al. (2016). Tractography-based connectomes are dominated by false-positive connections. *bioRxiv*, (p. 084137).
- Neher, P. F., Laun, F. B., Stieltjes, B., & Maier-Hein, K. H. (2014). Fiberfox: facilitating the creation of realistic white matter software phantoms. *Magnetic resonance in medicine*, *72*, 1460–1470.
- Parker, G. J., & Alexander, D. C. (2003). Probabilistic Monte Carlo based mapping of cerebral connections utilising whole-brain crossing fibre information. In *Biennial International Conference on Information Processing in Medical Imaging* (pp. 684–695). Springer.
- Peterson, P. (2009). F2PY: a tool for connecting Fortran and Python programs. *International Journal of Computational Science and Engineering*, *4*, 296–305.
- Poupon, C., Laribière, L., Tournier, G., Bernard, J., Fournier, D., Fillard, P., Descoteaux, M., & Mangin, J. (2010). A diffusion hardware phantom looking like a coronal brain slice. In *Proceedings of the International Society for Magnetic Resonance in Medicine* (p. 581). volume 18.
- Reisert, M., Kellner, E., & Kiselev, V. G. (2012). About the geometry of asymmetric fiber orientation distributions. *IEEE transactions on medical imaging*, *31*, 1240–1249.
- Sotiropoulos, S. N., Bai, L., Morgan, P. S., Constantinescu, C. S., & Tench, C. R. (2010). Brain tractography using Q-ball imaging and graph theory: Improved connectivities through fibre crossings via a model-based approach. *NeuroImage*, *49*, 2444–2456.
- Staudt, C., Sazonovs, A., & Meyerhenke, H. (2014). Networkkit: An interactive tool suite for high-performance network analysis. *CoRR*, abs/1403.3005, .
- Tournier, J. D., Calamante, F., & Connelly, A. (2007). Robust determination of the fibre orientation distribution in diffusion MRI: Non-negativity constrained super-resolved spherical deconvolution. *NeuroImage*, *35*, 1459–1472.
- Tournier, J. D., Calamante, F., & Connelly, A. (2010). Improved probabilistic streamlines tractography by 2nd order integration over fibre orientation distributions. *Proceedings of the International Society for Magnetic Resonance in Medicine*, (p. 1670).
- Tournier, J. D., Calamante, F., & Connelly, A. (2012). MRtrix: Diffusion tractography in crossing fiber regions. *International Journal of Imaging Systems and Technology*, *22*, 53–66. doi:10.1002/ima.22005.
- Van Essen, D. C., & Ugurbil, K. (2012). The future of the human connectome. *NeuroImage*, *62*, 1299–1310.
- Wedgeen, V. J., Hagmann, P., Tseng, W.-Y. I., Reese, T. G., & Weisskoff, R. M. (2005). Mapping complex tissue architecture with diffusion spectrum magnetic resonance imaging. *Magnetic Resonance in Medicine*, *54*, 1377–1386.
- Wedgeen, V. J., Wang, R. P., Schmahmann, J. D., Benner, T., Tseng, W. Y. I., Dai, G., Pandya, D. N., Hagmann, P., D'Arceuil, H., & de Crespigny, A. J. (2008). Diffusion spectrum magnetic resonance imaging (DSI) tractography of crossing fibers. *NeuroImage*, *41*, 1267–1277.
- Yeh, F.-C., Verstynen, T. D., Wang, Y., Fernández-Miranda, J. C., & Tseng, W.-Y. I. (2013). Deterministic diffusion fiber tracking improved by quantitative anisotropy. *PLoS one*, *8*, e80713.
- Yeh, F.-C., Wedeen, V. J., & Tseng, W.-Y. I. (2010). Generalized q-Sampling Imaging. *IEEE Transactions on Medical Imaging*, *29*, 1626–1635.
- Zalesky, A. (2008). DT-MRI fiber tracking: a shortest paths approach. *IEEE transactions on medical imaging*, *27*, 1458–1471.
- Zalesky, A., & Fornito, A. (2009). A DTI-Derived Measure of Cortico-Cortical Connectivity, . (pp. 1–15).

## Supplementary Materials

### 4.1. Implementation details

We implemented analytic tractography as a Python (3.3+) package. **MITTENS** functionality can be split into two areas. Equations 4 and 6 are implemented as Fortran90 extension modules (Peterson, 2009). By default **MITTENS** includes Fortran code to calculate transition probabilities for the maximum turning angle and step size used throughout this manuscript. **MITTENS** can easily generate extension modules for other parameter choices.

**MITTENS** can read output from DSI Studio, which can reconstruct DTI, HARDI and DSI and apply a number of deconvolution algorithms. We recommend reconstructing and inspecting data for quality in DSI Studio before analysis with **MITTENS**. Once a satisfactory reconstruction is saved **MITTENS** reads in the **fib.gz** file and calculates transition probabilities from all available voxels and their neighbors. The **fib.gz** format is a MATLAB file with a specific set of variables describing the spatial extent of the data, voxel-size, anisotropy scalars and ODF data sampled on a standardized icosahedron. Effort is currently underway to also load results from reconstructing in DiPy (Garyfallidis et al., 2014) and MRTRIX (Tournier et al., 2010). Transition probabilities can be saved as a sparse matrix in MATLAB format or a series of NIfTI-1 image files. Calculating single-ODF and double-ODF transition probabilities then takes approximately 27 minutes on a single cpu. This calculation only needs to be performed once per reconstructed dataset, after which the probabilities can be loaded directly into a graph object. Our software uses **networkkit** (Staudt et al., 2014), a top performing scalable graph library (Koch et al., 2016), to store and search through the voxel graph.

### Algorithm stability

We show in Figure S1 that our recursive algorithm behaves predictably. Empty bars in these plots indicate that the algorithm failed to terminate for the corresponding pair of step size and  $\theta_{max}$ . This behavior is not a limitation but is actually ideal, as these particular parameter pairs produce biologically-implausible paths. We see that the number of turning angle sequences (i.e. the number of elements in  $\Sigma$ ) increases exponentially as step size goes down or  $\theta_{max}$  increases. The estimated transition probabilities to edge and corner neighbors increases as step size increases. Intuitively, this is a consequence of a step being able to hop into neighboring edge or corner voxels from deeper in the source voxel without first landing in one of the 6 face-sharing neighbors – resulting in larger potential starting cuboids ( $\mathcal{V}$ ) for those turning angle sequences.

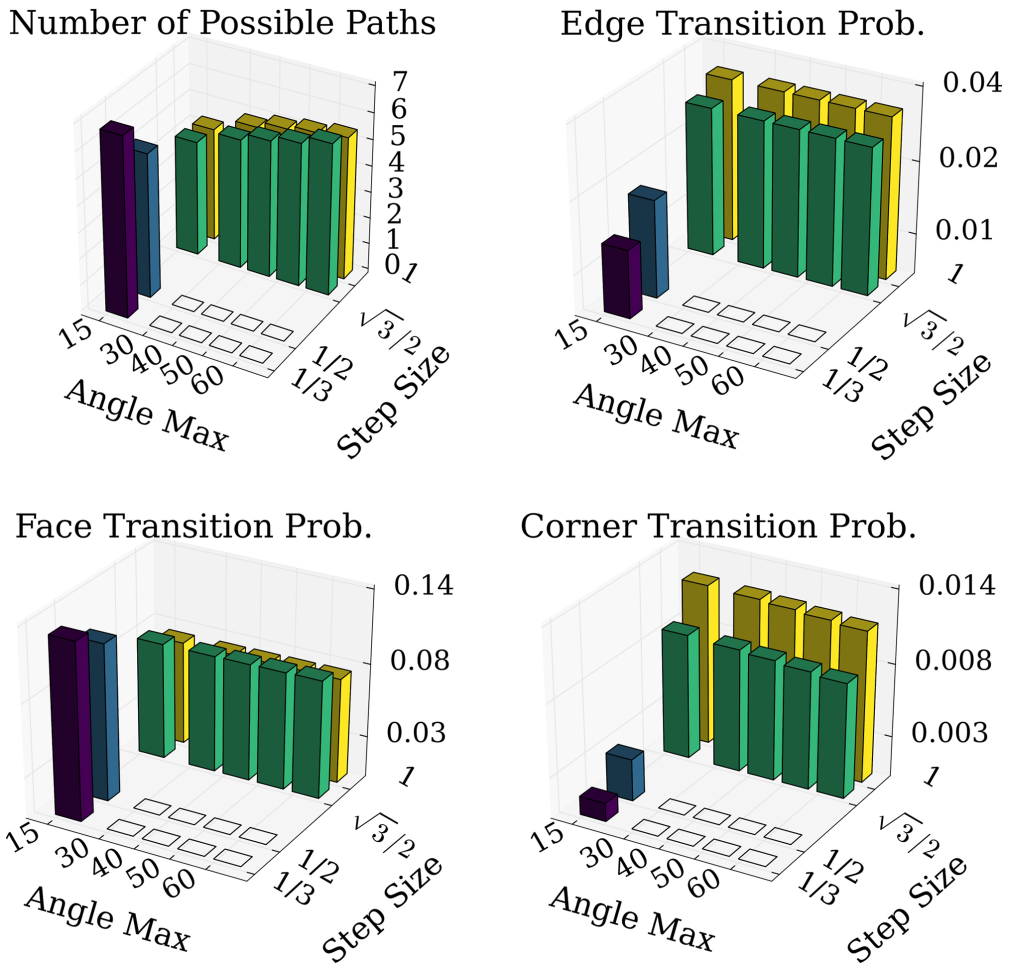


Figure S1: Transition probabilities for an isotropic ODF are plotted as a function of step size and maximum turning angle. The  $z$  axis of the top left plot is in  $\log_{10}$ .

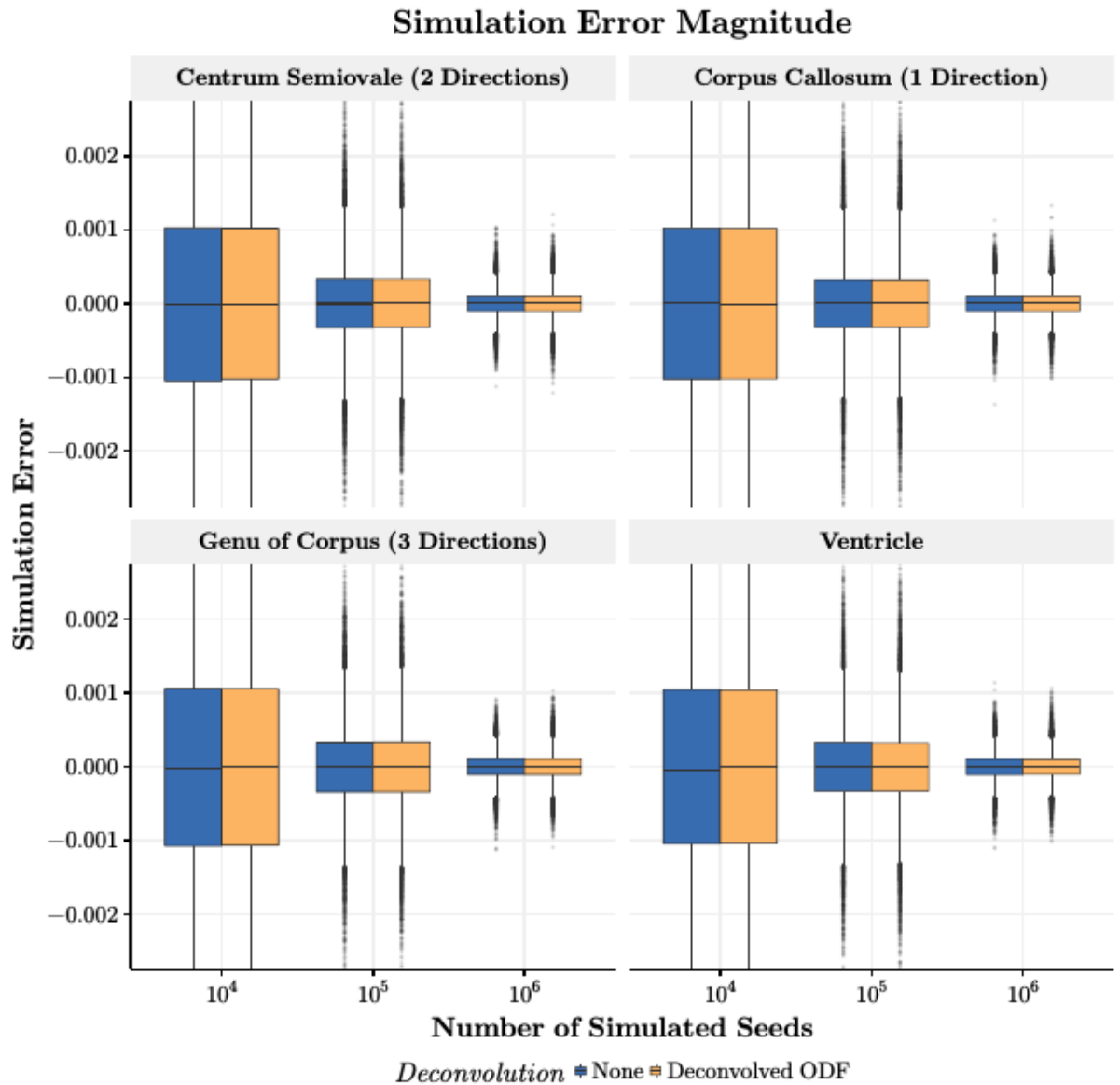


Figure S2: Distributions of the magnitude of simulation-related error as a function of the number of simulated seeds. Each panel depicts a voxel from Figure 3. ODFs came from a high-quality DSI dataset.

*Source regions used for tractography*

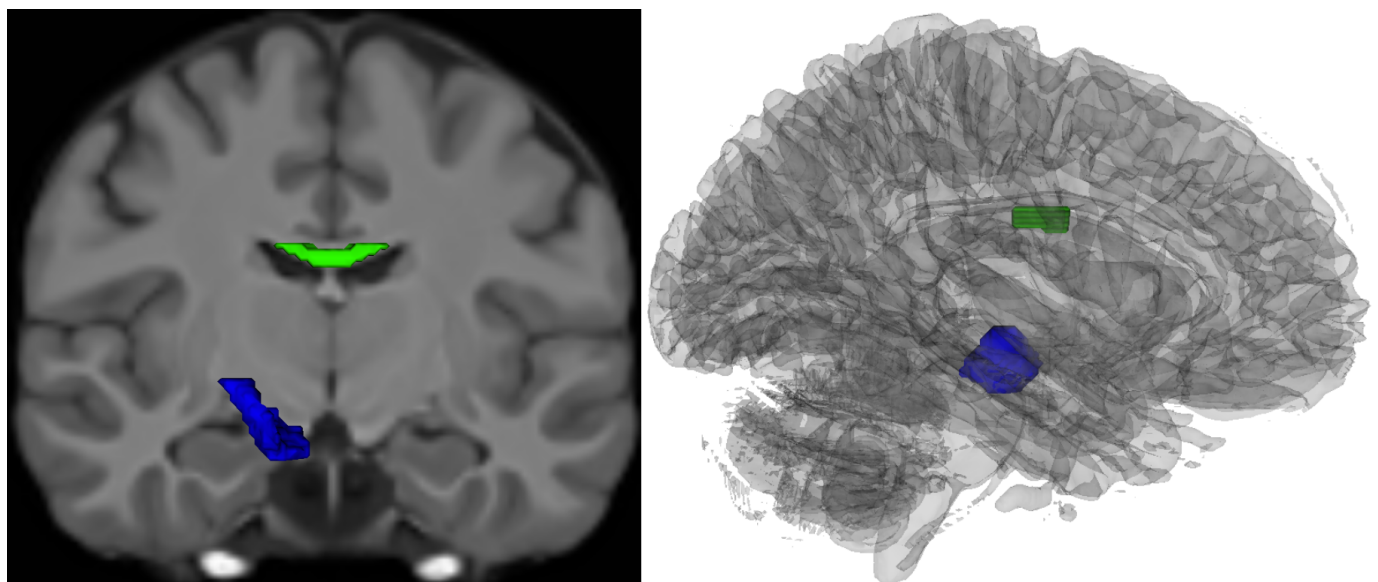


Figure S3: The corpus callosum source region (green) and cerebral peduncle regions are plotted along with the T1-weighted image from the group template. Left shows the regions as 3D surfaces and right shows the regions inside a 3D rendering of the template brain.

*Additional slice views and thresholds for tractography comparison*

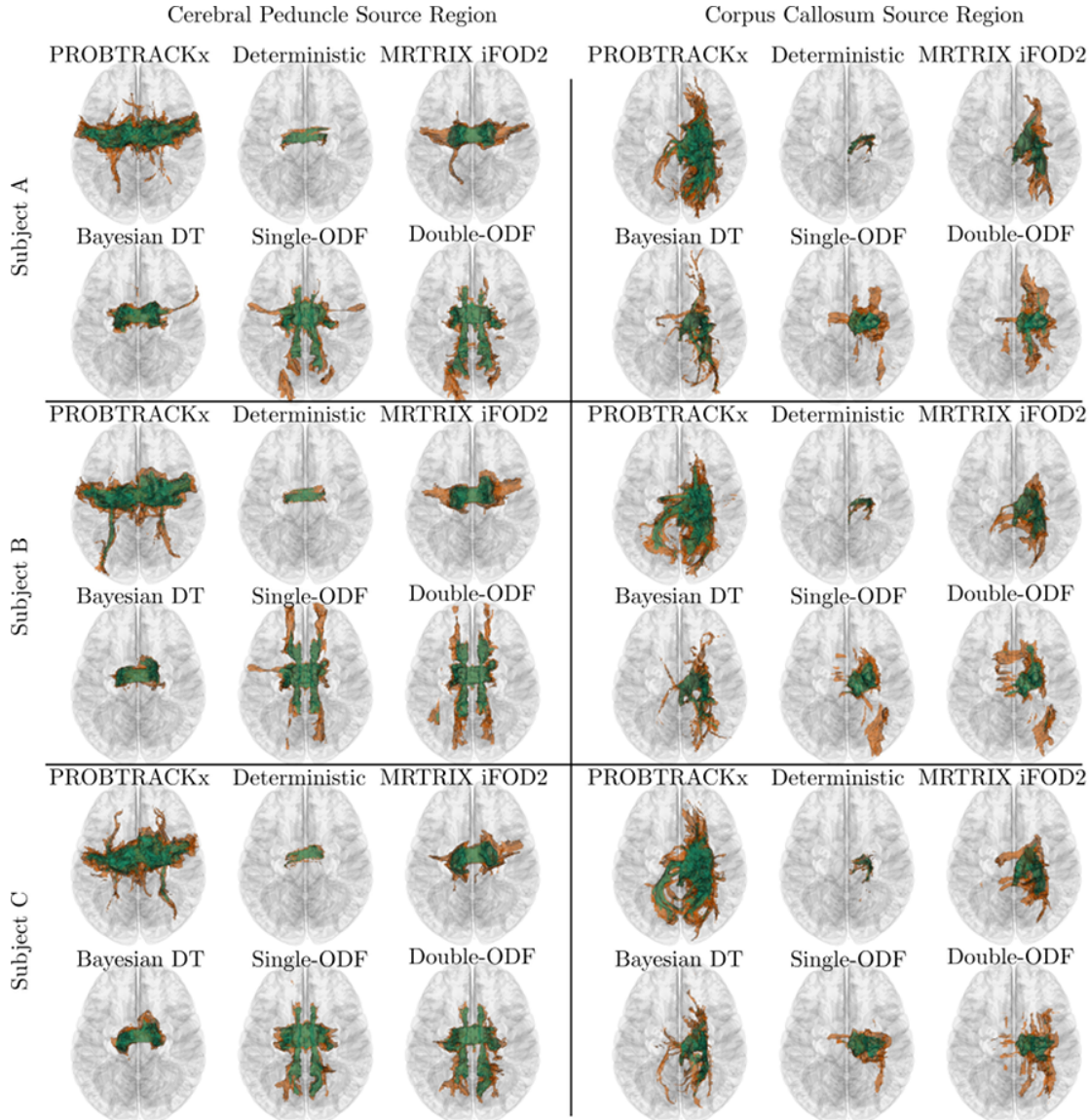


Figure S4: Tractography results from three HCP subjects. Voxels in the having the top 5% of connectivity scores are enclosed in an orange surface and the top 2% are enclosed in a green surface. The tractography method used to generate the map is listed above the brain images. Images in the left panels are the result of tracking from the cerebral peduncle ROI, and the right result from tracking from the corpus callosum ROI. This view is from the top of the brain facing downwards.